Electronic Supplementary Information (ESI) for

Cobalt-free layered perovskites *R*BaCuFeO$_{5+\delta}$ (R = 4*f* lanthanide) as electrocatalysts for the Oxygen Evolution Reaction

Elena Marelli, ‡[a,b] Jike Lyu, ‡[a] Mickaël Morin[a,c], Maxime Leménager[a], Tian Shang[a,d], N. Sena Yüzbasi[e], Dino Aegerter[b], Jinzhen Huang[b], Niéli D. Daffé[f], Adam H. Clark[g], Denis Sheptyakov[h], Thomas Graule[e], Maarten Nachtegaal[g], Ekaterina Pomjakushina[a], Thomas J. Schmidt[b,i], Matthias Krack[j,*], Emiliana Fabbri[b,*], and Marisa Medarde[a,*]

a. Laboratory for Multiscale Materials Experiments, Paul Scherrer Institut, CH-5232 Villigen PSI
b. Electrochemistry Laboratory, Paul Scherrer Institut, CH-5232 Villigen PSI
c. Excelsus Structural Solutions (Swiss) AG, PARK InnovAARE, CH-5234 Villigen PSI
d. Key Laboratory of Polar Materials and Devices (MOE), School of Physics and Electronic Science, East China Normal University, Shanghai, China
e. High Performance Ceramics, EMPA, Swiss Federal Laboratories for Materials Science and Technology, CH-8600 Dübendorf
f. Laboratory for Condensed Matter, Paul Scherrer Institut, CH-5232 Villigen PSI
g. Laboratory for Synchrotron Radiation and Femtochemistry, Paul Scherrer Institut, CH-5232 Villigen PSI
h. Laboratory for Neutron Scattering and Imaging, Paul Scherrer Institut, CH-5232 Villigen PSI
i. Laboratory of Physical Chemistry, ETH Zürich, CH-8093 Zürich
j. Laboratory for Materials Simulations, Paul Scherrer Institut, CH-5232 Villigen PSI.
‡ These authors contributed equally to this work
* Corresponding authors
† Electronic Supplementary Information (ESI) available. See DOI: 10.1039/x0xx00000x

This PDF file includes:

- Materials and Methods
- Figures. S1 to S16
- Tables S1 to S3
- References (1–17)

Materials and Methods

Sample synthesis

The *R*BaCuFeO$_{5+\delta}$ ceramic samples with *R* = La, Pr, Nd, Eu, Gd, Tb, Dy, Ho, Er, Tm, Yb and Lu were prepared by solid-state synthesis with the aim of obtaining powders with large particle sizes and homogeneous particle size distributions. To reach this goals, a particular attention to the synthesis protocol. Besides employing identical precursor mixing times, annealing times and cooling down procedures, we used the same (tubular) furnace for all the samples, which was recalibrated at the beginning of the study in order to identify the region with the best temperature homogeneity. High-purity R_2O_3 ($R \neq$ Tb, Pr) Tb_4O_7 and Pr_6O_{11} (99.995 to 99.998%; Aldrich/Alfa Aesar), $BaCO_3$ (99.997%; Alfa Aesar), CuO (99.995%; Alfa Aesar), and Fe_2O_3 (99.998%; Alfa Aesar) powders were used as starting materials. Dehydrated rare-earth oxide powders were obtained by heating the commercial materials at 1223 K for 10 hours. The required stoichiometric amounts of R_2O_3, Tb_4O_7, Pr_6O_{11}, $BaCO_3$, CuO, and Fe_2O_3 were weighted, thoroughly grounded in an automatic Agatha mortar during 1 hour and heated up to the synthesis temperature T_s (1323 to 1430 K, depending on the *R* cation). The powders were then annealed for 50 hours under oxygen gas flow (75 ml/min), cooled down to room temperature (RT), grounded again for 45 min, pressed into pellets, and sintered at T_s for another 50 hours. The cooling rate after each annealing was 300 K/h.

The nano- LaBaCuFeO$_{5+\delta}$ sample was prepared by flame-spray synthesis, as described in refs.[1, 2]. Stoichiometric amounts of lanthanum nitrate ($La(NO_3)_{3\cdot x}H_2O$, 99.9 %, Sigma-Aldrich, Buchs, Switzerland), barium carbonate ($BaCO_3$, ≥ 99.0%, Sigma-Aldrich, Buchs, Switzerland), copper nitrate ($Cu(NO_3)_2 \cdot 3H_2O$, ≥ 99.0%, Sigma-Aldrich, Buchs, Switzerland) and iron nitrate nonahydrate ($Fe(NO_3)_2$ $9H_2O$, ≥ 98%, Sigma-Aldrich, Buchs, Switzerland) were dissolved in a solvent mixture of ultrapure water (MicroPure UV, Thermo Fisher Scientific, Reinach, Switzerland) and acetic acid (AcOH, ≥99.0%, Carl Roth, Arlesheim, Switzerland) with a 75:25 volume ratio. The total metal concentration of the final precursor solution was 0.1 M. The solution was injected continuously into the spraying nozzle via a flow-controlled three-piston pump (C-610, Büchi, Flawil, Switzerland) with a flowrate of 50 mL·min^{-1}.

Powder X-ray diffraction and particle size determination

The sample purity of all samples was checked with laboratory powder X-ray diffraction (PXRD) using a Brucker D8 Advance diffractometer (Cu K_α). Powder diffraction patters were measured for all samples at room temperature (RT) and analysed using the Rietveld method as implemented in the FullProf Suite package.[3] All ceramic powders were free of impurities within the limit of this technique (~1%) and very well crystallized. In the case of the $LaBaCuFeO_{5+\delta}$ nanopowder, PXRD revealed the presence of the nominal phase (majority), minor amounts of $Cu(NO_3)_2$ and $Ba(NO_3)_2$, and traces of $LaBa_2Cu_3O_{6+\delta}$ and BaO_2 (Fig. S16). The average particle size was estimated using the Scherrer formula $D = \lambda / \beta\,(hkl) \cos\theta$, as implemented in the FullProf Suite software. Here, β is the integral width of the Bragg reflections corrected from the instrumental resolution, and D is the mean size of the crystalline domains. Such domains may be either equal or smaller than the grain size, which may also be equal or smaller than the particle size. The obtained D values, listed in Table S2, provide thus a lower limit to the actual average particle size.

Complementary, SEM images were obtained for all samples, including the $LaBaCuFeO_{5+\delta}$ nanopowder. This technique probes only a tiny sample portion, but provides real-space information on the actual particle shape and size. The SEM images, obtained using a Carl Zeiss Ultra 55 SEM microscope operating with 10 keV incident electron beam energy, and using the in-lens SE (Secondary Electron) detector, are shown in Fig. S5. They reveal a tendency towards platelet-like habit, consistent with the layered nature of the materials investigated, as well as comparable particle size distributions for the ceramic samples. As expected, the particle sizes in the obtained images were in general larger than the values estimated from the Scherrer formula.

Electrochemical measurements and specific-surface area

A standard three-electrode Teflon cell was used to measure the room-temperature electrochemical activity of the $R BaCuFeO_{5+\delta}$ catalysts in air-saturated 0.1 M KOH. The catalysts inks were prepared by sonicating 2.5 ml of solvent mixture (composed of Milli-Q water : isopropyl alcohol (Sigma Aldrich, 99.999%): Na^+-exchanged Nafion (Sigma-Aldrich, 5 wt%) in the 1:4:0.02 ratio) per mg of catalyst powder. The freshly sonicated suspension, with a 0.02 mg catalyst content was drop-casted on a polished

glassy-carbon electrode (D = 5 mm). A gold mesh and an Hg/HgO (Re-61AP, ALS, Japan) electrode were used as counter and reference electrodes respectively. The reference electrode was calibrated in a hydrogen-saturated electrolyte against a polycrystalline Pt insert ($V_{Hg/HgO} = V_{RHE}$ - 0.934 V). The measurement protocol includes 25 cyclic voltammetry (CV) measurements between 1 and 1.7 V_{RHE} at 10 mV s^{-1} scan rate, followed by chronoamperometric measurements in the 1.3 to 1.7 V_{RHE} range, holding the potential for 30 s to reach steady-state conditions. Electrochemical impedance spectroscopy measurements evaluated the Ohmic drop at the beginning and end of the protocol at 1.2 and 1.4 V_{RHE}. For the ceramic samples, the 25th CV measurements (scan rate v = 0.01 V s^{-1}) were used for the calculation of the double layer capacitance C_{dl}. The potential window was set to 1 to 1.3 V vs. RHE (U_d = 0.3 V), and the area A of the CV curve within these limits was calculated numerically. The double layer capacitance was then calculated as $C_{dl} = A / (U_d * v)$.

The catalysts' specific surface area of the ceramic and nano-sized $LaBaCuFeO_{5+\delta}$ samples were evaluated with the Brunauer-Emmett-Teller (BET) analysis using N_2 desorption isotherms (AUROSORB-1, Quantachrome).

Electric conductivity

The RBaCuFeO$_{5+\delta}$ samples ex-situ electric conductivity was obtained through 4-wire room temperature electrochemical impedance spectroscopy (EIS) measurements (see Fig. S2b for a representative measurement). The powder samples were kept at constant pressure (0.6 MPa) in a homemade measurement setup and the EIS was measured between 1 MHz and 1 Hz, applying a 100 mV bias. The electric conductivity was calculated as $\sigma = L / RA$ where R is the Ohmic resistance obtained as intercept of the Nyquist plot with the real axis whereas L and A are respectively the thickness and area of the measured sample. In our setup $A = \pi R^2$, with R = 0.5 cm, and the sample thickness L depends on the amount of material used (typically between 0.1 and 0.25 mm).The conductivity was obtained as average of at least three measurements at different thicknesses. A representative measurement is shown in Fig. S2b.

Powder neutron diffraction

Powder neutron diffraction (PND) measurements were carried out at the Swiss Spallation Neutron Source (SINQ) of the Paul Scherrer Institut in Villigen, Switzerland. High-resolution powder diffraction patterns were recorded for the samples with *R* = Tb, Nd, Pr and La at the powder diffractometer HRPT.[4] The samples were loaded in cylindrical vanadium cans (D = 6 mm, H = 50 mm) and mounted on a He cryostat stick. To reduce the background noise, the empty section of the cans was shielded with Cd foil, and an oscillating radial collimator was used to eliminate the sample environment signal. The samples were measured at RT with wavelength of λ = 1.15 Å. The instrumental parameters were refined using a $Na_2Al_{12}Ca_3F_{14}$ (NAC) reference sample collected in the same conditions. For the materials with *R* = Eu and Gd, the large neutron absorption cross section of these lanthanides prevented the use of PND. Laboratory powder X-ray diffraction patterns with improved resolution and statistics were thus recorded for these samples at RT.

Structural analysis

All powder neutron diffraction data were analysed using the Rietveld package FullProf Suite[3] , freely available at https://www.ill.eu/sites/fullprof/. Two space groups can be used to describe the tetragonal crystal structure depending on whether the Cu/Fe distribution is centrosymmetric (*P4/mmm*) or non-centrosymmetric (*P4mm*).[5] Since the degree of disorder in these materials is often close to 50% - 50%,[6-9] both space groups give usually very similar results. However, the special positions of Ba, Nd, O1 and O3 in *P4/mmm* (Table S3) provide an increased stability to the Rietveld fits with this space group, in particular for the structural refinements of medium resolution PXRD laboratory data. Moreover, in the case of high-resolution PND, its use results in a higher sensitivity to the occupation of the different oxygen positions, relevant for the samples with the larger lanthanides. For $TbBaCuFeO_5$, with $\delta = 0$, we employed thus the non-centrosymmetric space group *P4mm* already used in our previous study on stoichiometric $RBaCuFeO_5$ compounds with *R* = Lu to Dy,[7] which confirmed a Fe/Cu occupation close to 50%-50%. For *R* = Gd to La we used the centrosymmetric space group *P4/mmm* instead. Anisotropic Debye-Waller factors were used to fit the high-resolution PND data (*R* = Nd, Pr, La), and isotropic for the PXRD data (*R* = Gd, Eu). Due to the limited sensitivity of X ray to light atoms, and the

trend in the dependence of δ with the *R* ionic radius shown in Fig. 2e, the Gd and Eu samples were assumed to be stoichiometric ($\delta = 0$). The only free atomic coordinates were thus the *z* values of Cu, Fe and O2 (0.2855(4), 0.2502(7) and 0.3109(3) for Gd, and 0.2785(8), 0.258(1) and 0.3073(4) for Eu, respectively). For the $LaBaCuFeO_{5+\delta}$ sample prepared by flame spray, a *c/2a* ratio of 1.0057(1), very close that of the ceramic sample (1.00324(1), Table S2) indicates the presence of pseudocubicity and La/Ba intermixing. The distribution of the two cations between the two A-sites could however not be determined due to the broadening of the Bragg reflections in the PXRD patterns of the $LaBaCuFeO_{5+\delta}$ nanopowder. The slightly different values of the *a* and *c* lattice constants suggest however a different La/Ba distribution, and possibly, a different oxygen content.

X-ray absorption spectroscopy (XAS)

The Fe and Cu *K*-edges X-ray absorption spectroscopy (XAS) data of the $RBaCuFeO_{5+\delta}$ samples were collected at RT using the Total Fluorescence Yield mode (TFY) at the SuperXAS beamline[10] of the Swiss Light Source (SLS), Paul Scherrer Institut, using a Passivated Implanted Planar Silicon (PIPS) detector. Circa 5 mg of sample was diluted in 80 mg of cellulose and pressed in 13 mm pellets. The data treatment, including energy calibration, background removal and edge-step normalization, was performed using the software package ProQEXAFS, freely available via a Github repository at https://github.com/ClarkAH/ProQEXAFS-GUI.

The Cu and Fe $L_{3,2}$-edges, O *K*-edges, and $M_{5,4}$ Ba and *R*-cation edges were recorded at the X-Treme beamline[11] of the SLS at RT using the Total Electron Yield Mode (TEY). For the O K-edges, a second set of spectra was also recorded using the TFM. The powder samples were mechanically pressed into a thick, O-free indium foil that was mounted on a Cu holder. After subtracting a linear background, the *L* and *M*-edges were normalized to the maximum of the L_3 / M_5 line (the absolute spectra maximum in the case of the Lu *M*-edge). For the O *K* edges, the spectra were area-normalized between 520-565 eV after a linear background subtraction in order to compare the relative intensities of the different features.

Computational Methods

All electronic structure calculations have been performed using the *Vienna ab-initio simulation package VASP 5.4.4* [12, 13]. Supercells composed of $1 \times 1 \times 2$ unit cells with a volume of $\sqrt{2}\boldsymbol{a} \cdot \sqrt{2}\boldsymbol{a} \cdot 2\boldsymbol{c}$ were employed to model different stoichiometries of the $R\mathrm{BaCuFeO}_x$ $(x = 5, 5.5, 6)$ system using periodic boundary conditions (PBC). The Brillouin zone sampling was performed with a Γ-centered $8 \times 8 \times 4$ k point mesh and a Gaussian smearing of $\sigma = 0.05$ eV. A modified version of the exchange-correlation functional of Perdew, Burke, and Ernzerhof (PBE), named PBEsol[14], particularly suited for solid-state systems, was used in all calculations. The core electrons were described by projector augmented wave (PAW) potentials. The valence electrons (as given in brackets) of La $(5s^2\ 5p^6\ 6s^2\ 5d^1)$, Ba $(5s^2\ 5p^6\ \ 6s^2)$, Cu $(3p^6\ 3d^{10}\ 4s^1)$, Fe $(3s^2\ 3p^6\ 3d^7\ 4s^1)$, O $(2s^2\ 2p^4)$, and of all the $4f$elements *R*_3 from Pr to Lu were expanded by a plane wave cut-off energy of 600 eV. The PAW PBE potentials *R*_3 for the lanthanides keep the $4f$ electrons frozen in the core. A Hubbard *U* term as proposed by Dudarev et al.[15] was added (PBEsol+*U*) to account for the strongly correlated behaviour of the $3d$ electrons of Cu and Fe. Effective *U* values of 8 eV and 4 eV were applied for Cu and Fe, respectively. The cell parameters and the atomic positions within the cell were fully relaxed for all systems within the detected symmetry (C_{4v}) using a tight converge criteria (EDIFF 10^{-8}).

The O(2*p*) centroids for the occupied orbitals were calculated using the expression

$$E_{\mathrm{cent}}^{\mathrm{occ}}\big(\mathrm{O}(2p)\big) = \frac{\int_{-\infty}^{0} n(\epsilon)\ \epsilon\ d\epsilon}{\int_{-\infty}^{0} n(\epsilon)\ d\epsilon}$$

and likewise, the corresponding O(2p) centroids for the virtual (unoccupied) orbitals are computed using

$$E_{\mathrm{cent}}^{\mathrm{vir}}\big(\mathrm{O}(2p)\big) = \frac{\int_{0}^{\infty} n(\epsilon)\ \epsilon\ d\epsilon}{\int_{0}^{\infty} n(\epsilon)\ d\epsilon}$$

where n(ϵ) is the projected density of states (pDOS) of the occupied and virtual O(2p) orbitals for the energy ϵ, respectively. The data for plotting the density of states (DOS) and the projected DOS (pDOS) have been extracted from the VASP output files with `sumo-dosplot v1.0`.[16]

Figures S1 to S16

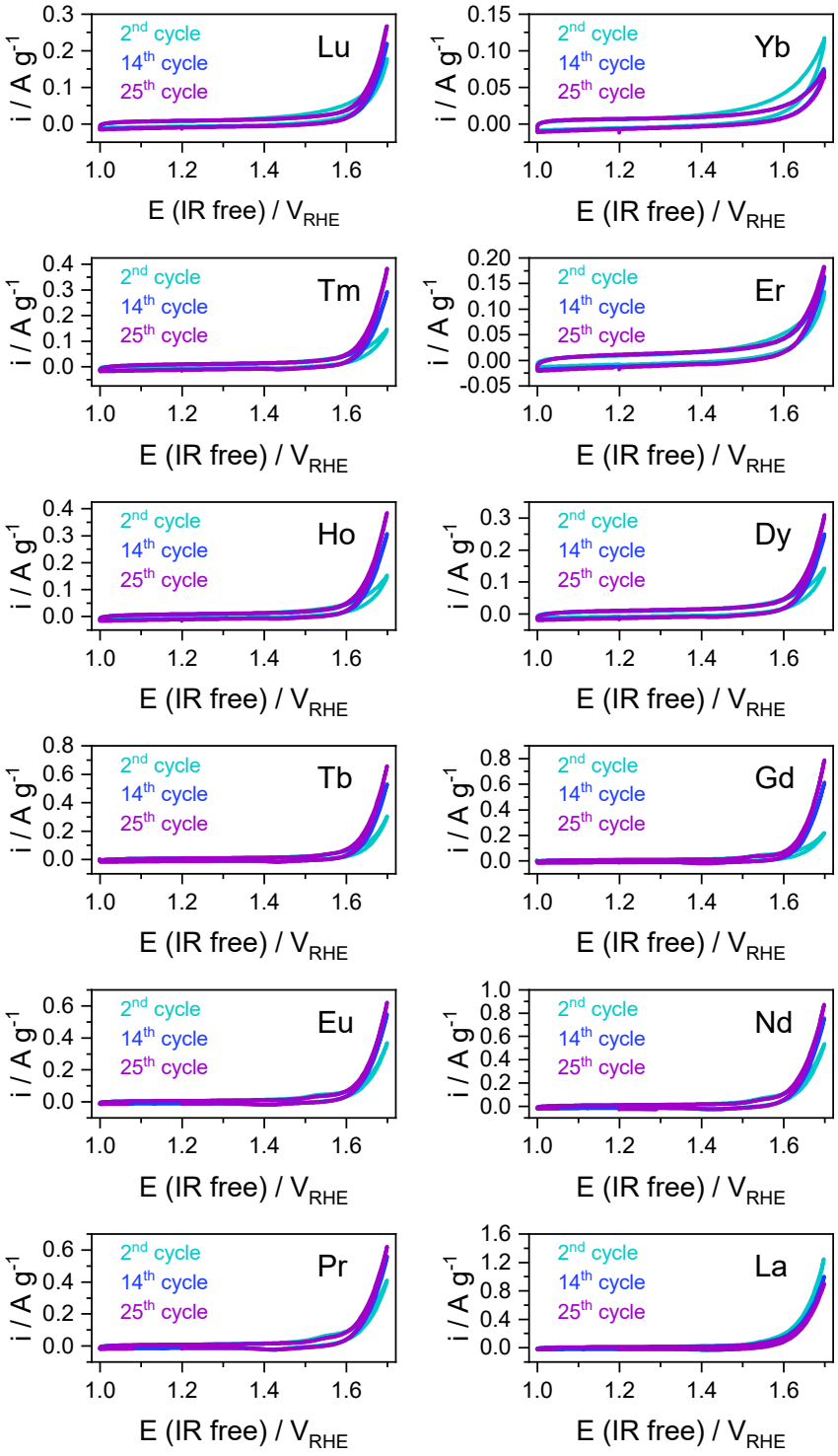

Fig. S1a. Cyclic voltammetry. Cyclic voltammograms of the *R*BaCuFeO$_{5+\delta}$ ceramic samples scanned at 10mV sec^{-1} between 1 and 1.7 V$_{RHE}$.

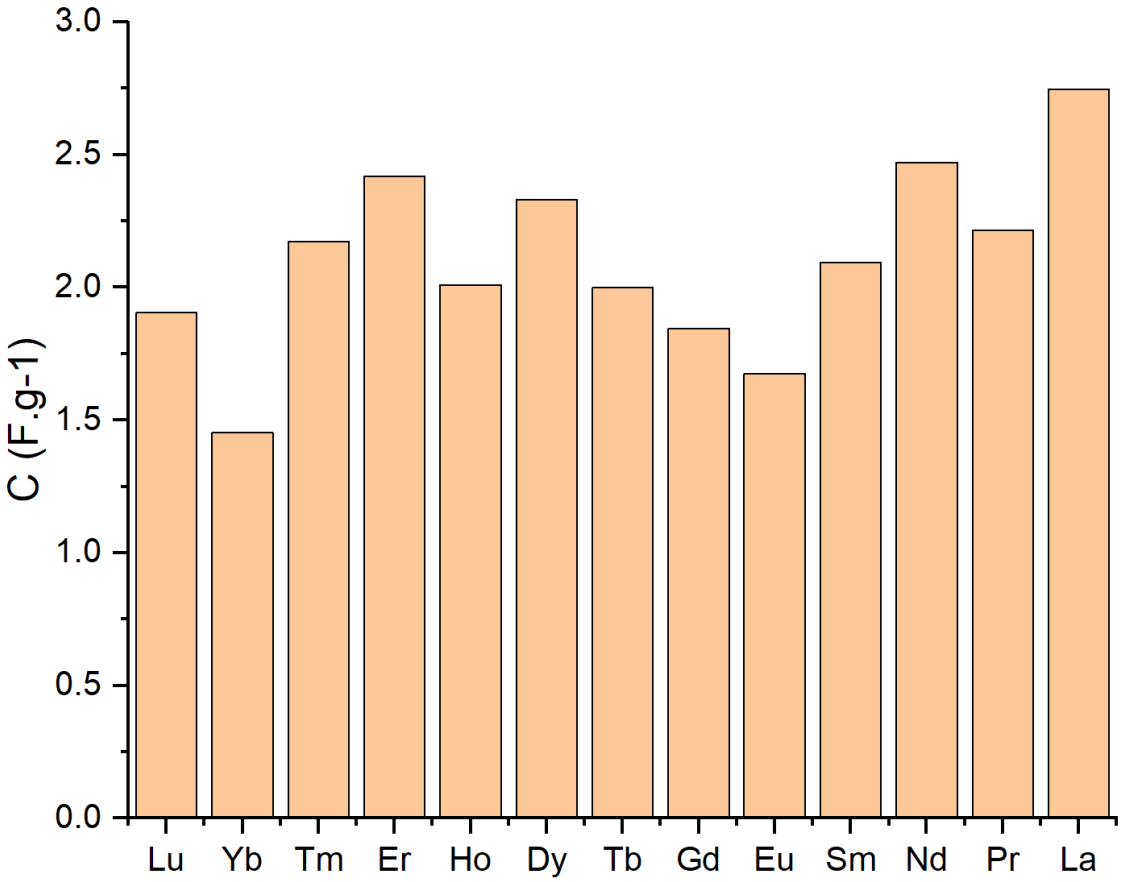

Fig. S1b. Double layer capacitance. Evolution of the double layer capacitance of the *R*BaCuFeO$_{5+\delta}$ ceramic samples with the *R* ionic radius.

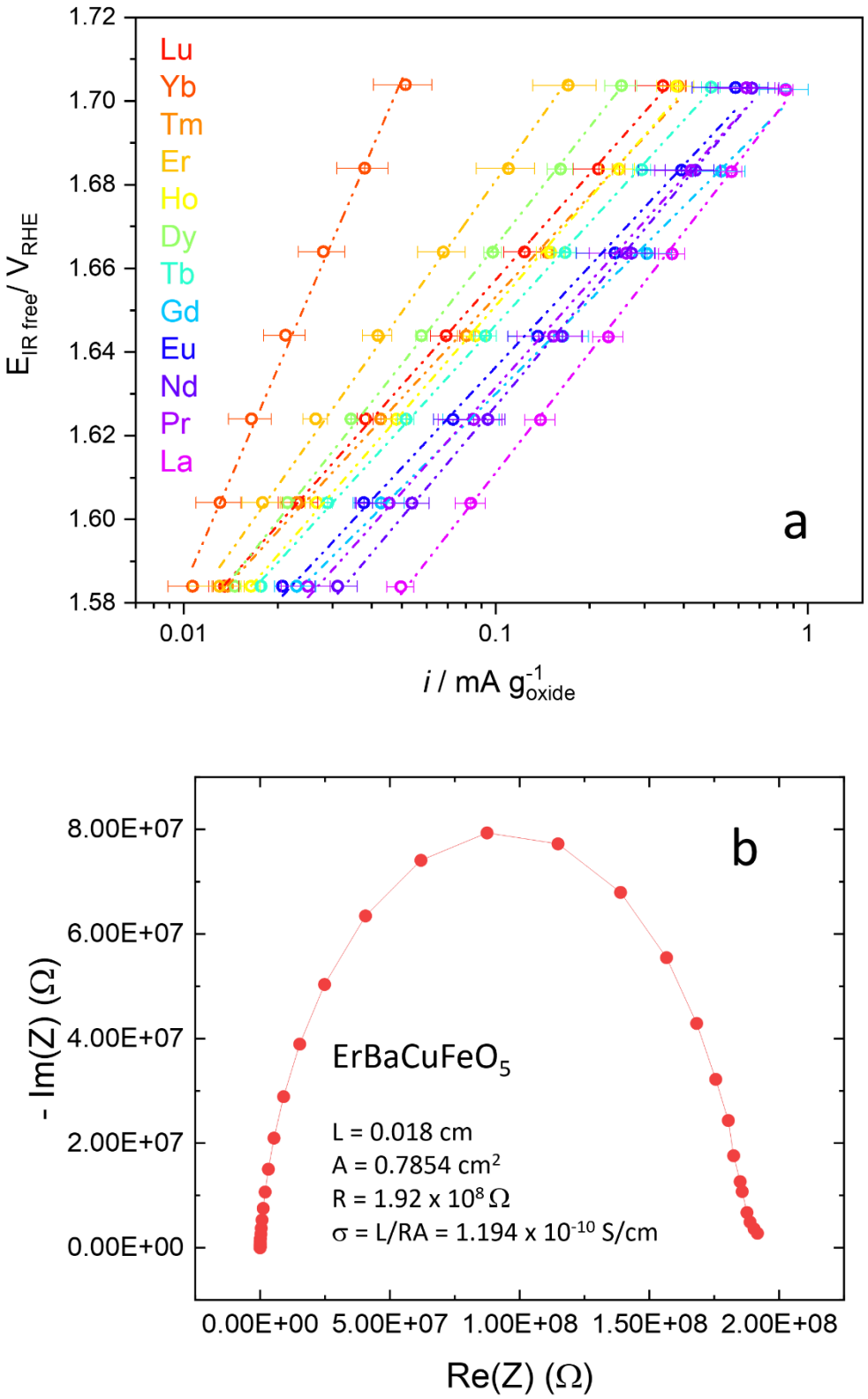

Fig. S2. Tafel plots and Impedance Spectroscopy. a) Oxygen Evolution Reaction Tafel plots of the *R*BaCuFeO$_{5+\delta}$ ceramic samples. b) Representative Impedance Spectroscopy measurement.

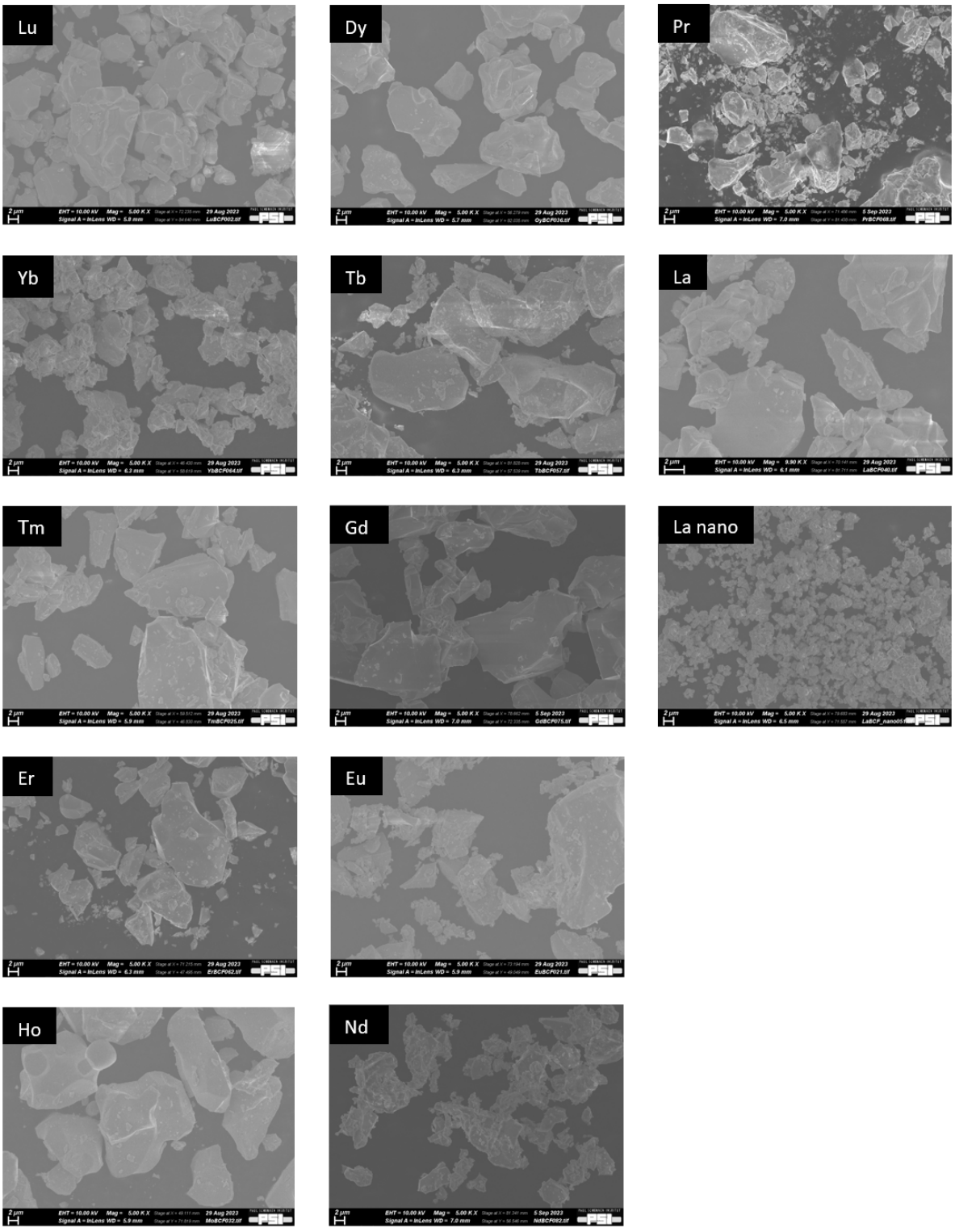

Fig. S3. **Particle size and morphology.** SEM images of the *R*BaCuFeO$_{5+\delta}$ ceramic samples and nanocrystalline LaBaCuFeO$_{5+\delta}$.

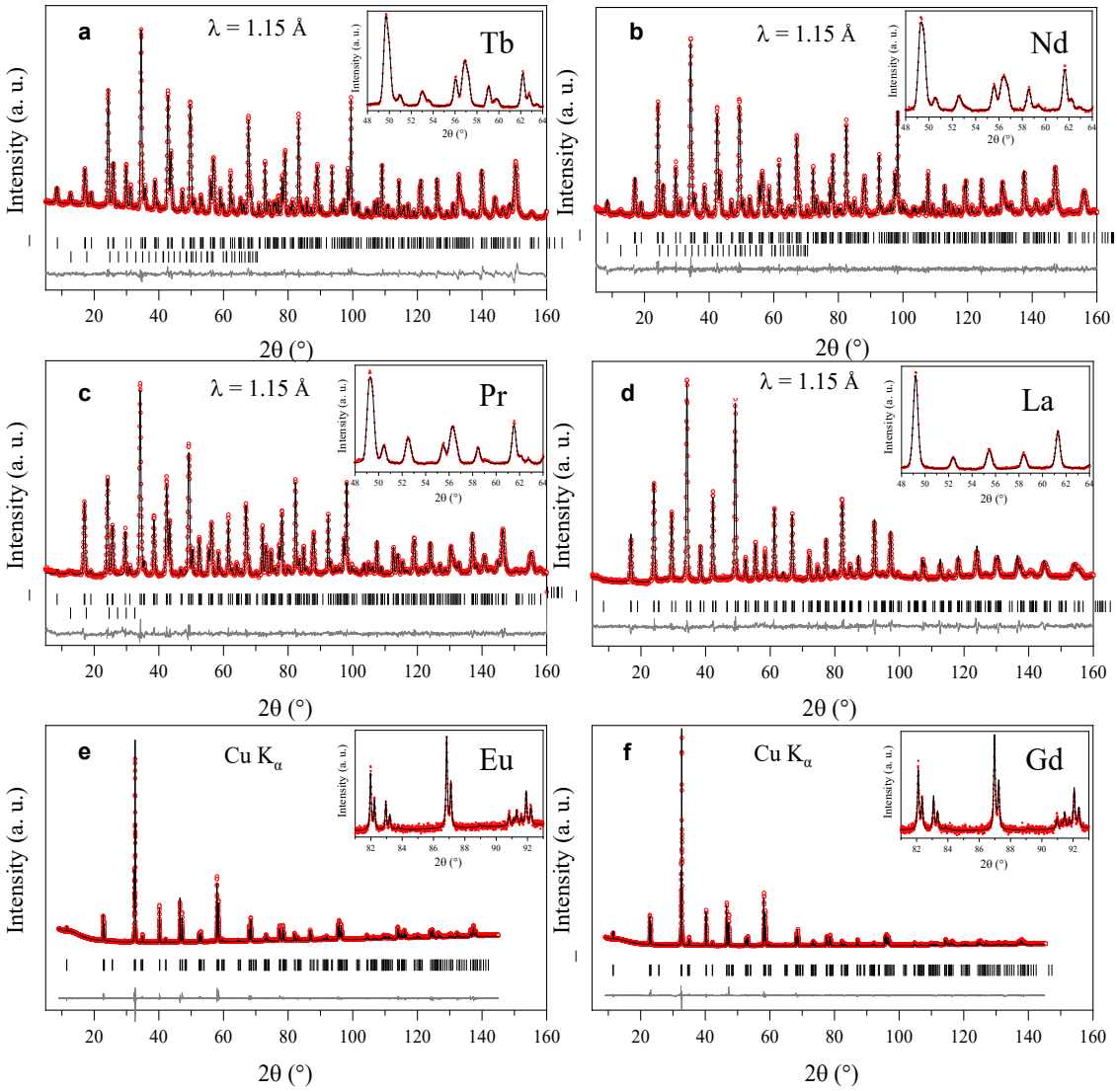

Fig. S4. Rietveld fits of the powder neutron diffraction (*R* = Tb, Nd, Pr, La) and X-ray powder diffraction (R = Gd, Eu) data. Red crosses: experimental data. Black lines: refined profiles. Grey lines: difference between the observed and calculated patters. Selected regions highlighting the agreement between the data and the calculation are shown in the insets. The first rows of ticks indicates the positions of the Bragg reflections associated to the tetragonal crystal structure. For *R* = Tb, Nd and Pr, the second row of ticks indicates the reflection positions associated to the collinear antiferromagnetic phase with **k** = (½ ½ ½).[6] The refined structural parameters are listed in Supplementary Tables 2 and 3. The PND patterns were measure at the high-resolution powder diffractometer HRPT[4] (SINQ, PSI), and the XRD data at a Brucker D8 Advance powder diffractometer.

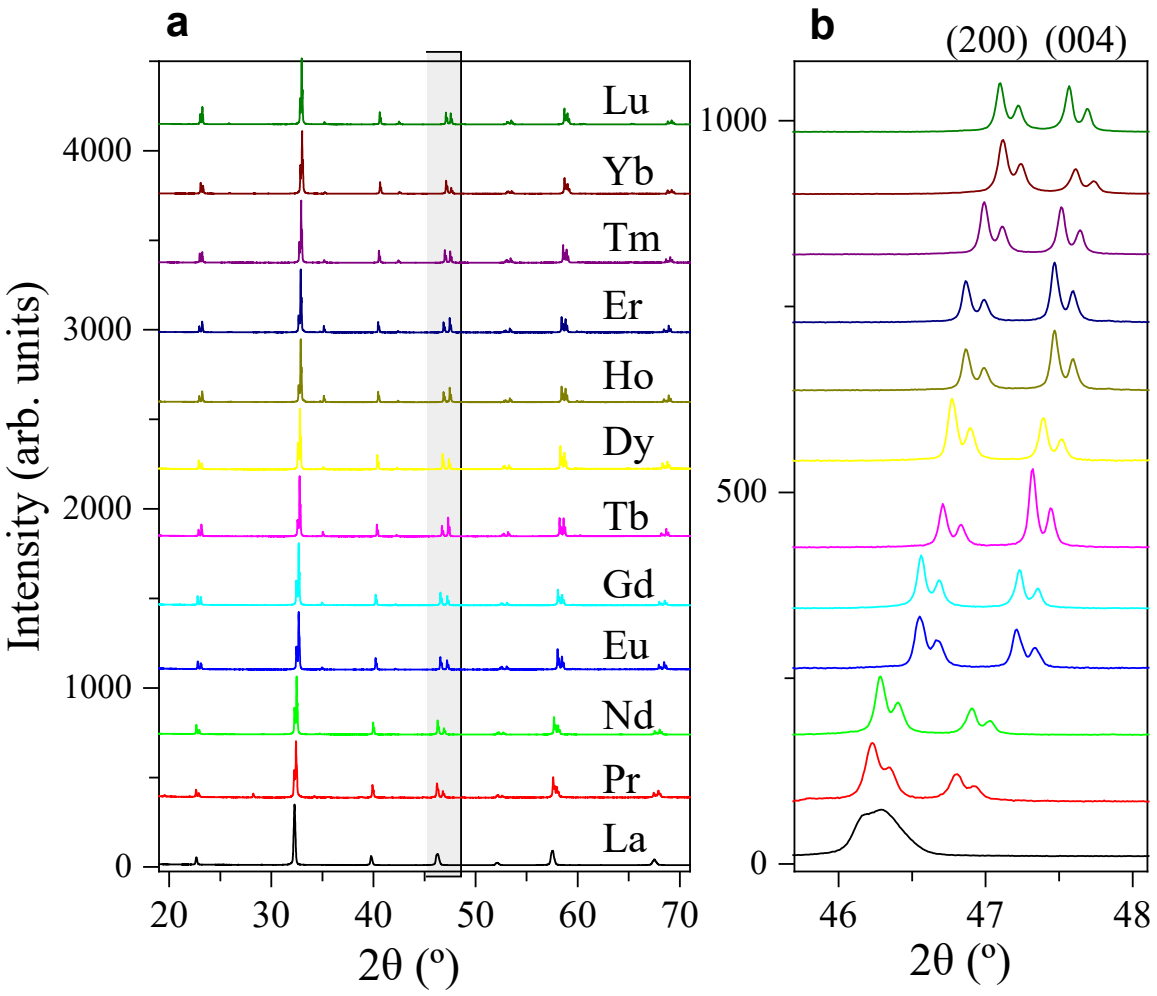

Fig. S5. Laboratory powder x-ray diffraction data. (a) Low angle region of the laboratory powder X-ray diffraction patterns (Cu K_α) measured at RT for the *R*BaCuFeO$_{5+\delta}$ ceramic samples. (b) Magnification of the shaded region in (a), highlighting the quasi-merging merging of the (200) and (004) Bragg reflections for pseudocubic LaBaCuFeO$_{5.49}$.

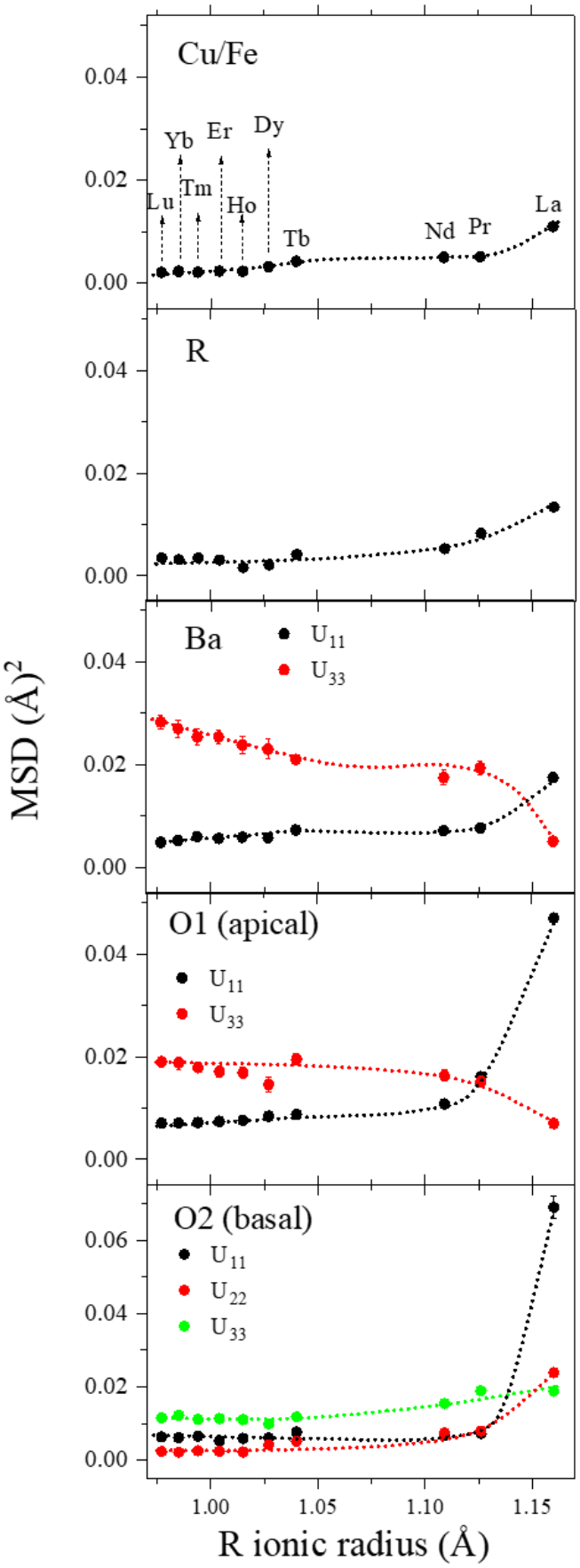

Fig. S6. Atomic Mean-Square Displacement parameters (MSD's) of the different atomic sites at RT. All values were obtained from the analysis of PND data measured on the high-resolution neutron powder diffractometer HPRT[4] (SINQ. PSI). *R* = Lu-Dy data are from ref.[7] *R* = Tb, Nd, Pr and La data are from this work. Dotted lines are guides for the eye.

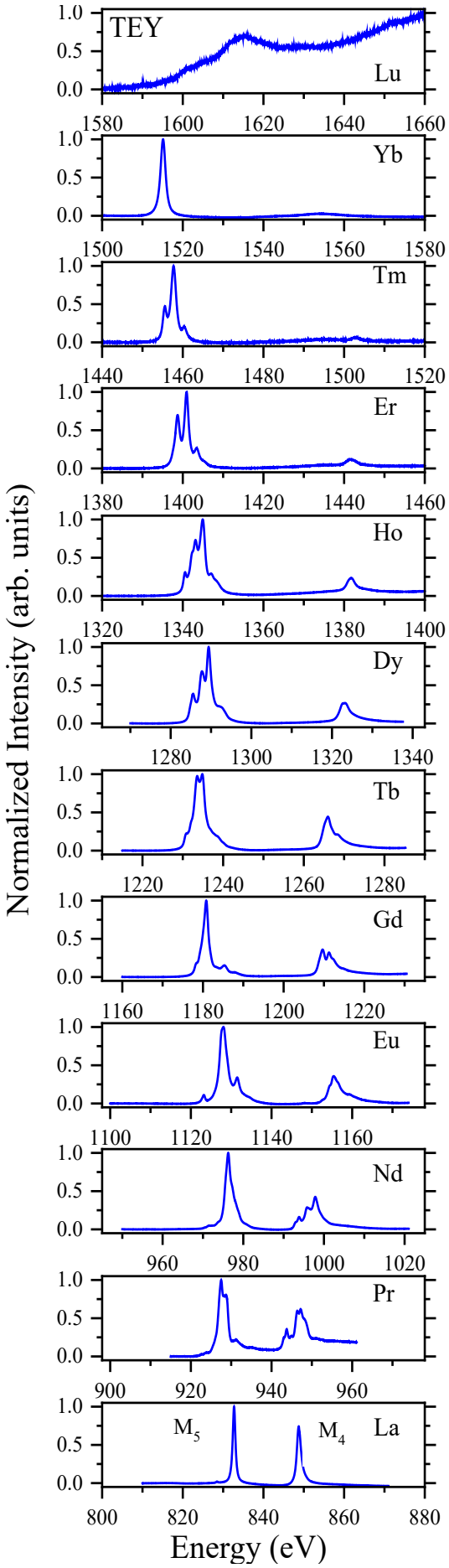

Fig. S7. ***4f* lanthanide *M*-edges of *R*BaCuFeO$_{5+\delta}$ layered perovskites**. All spectra were measured at the Xtreme beamline[11] (SLS, PSI) using the Total Electron Yield mode (TEY). For *R* = Pr, the $M_{5,4}$ edges are superimposed with the Cu $L_{3,2}$ edges (see also Fig. 5b and Fig. S9b). For comparison purposes, the energy span in the abscissa is the same for all the spectra.

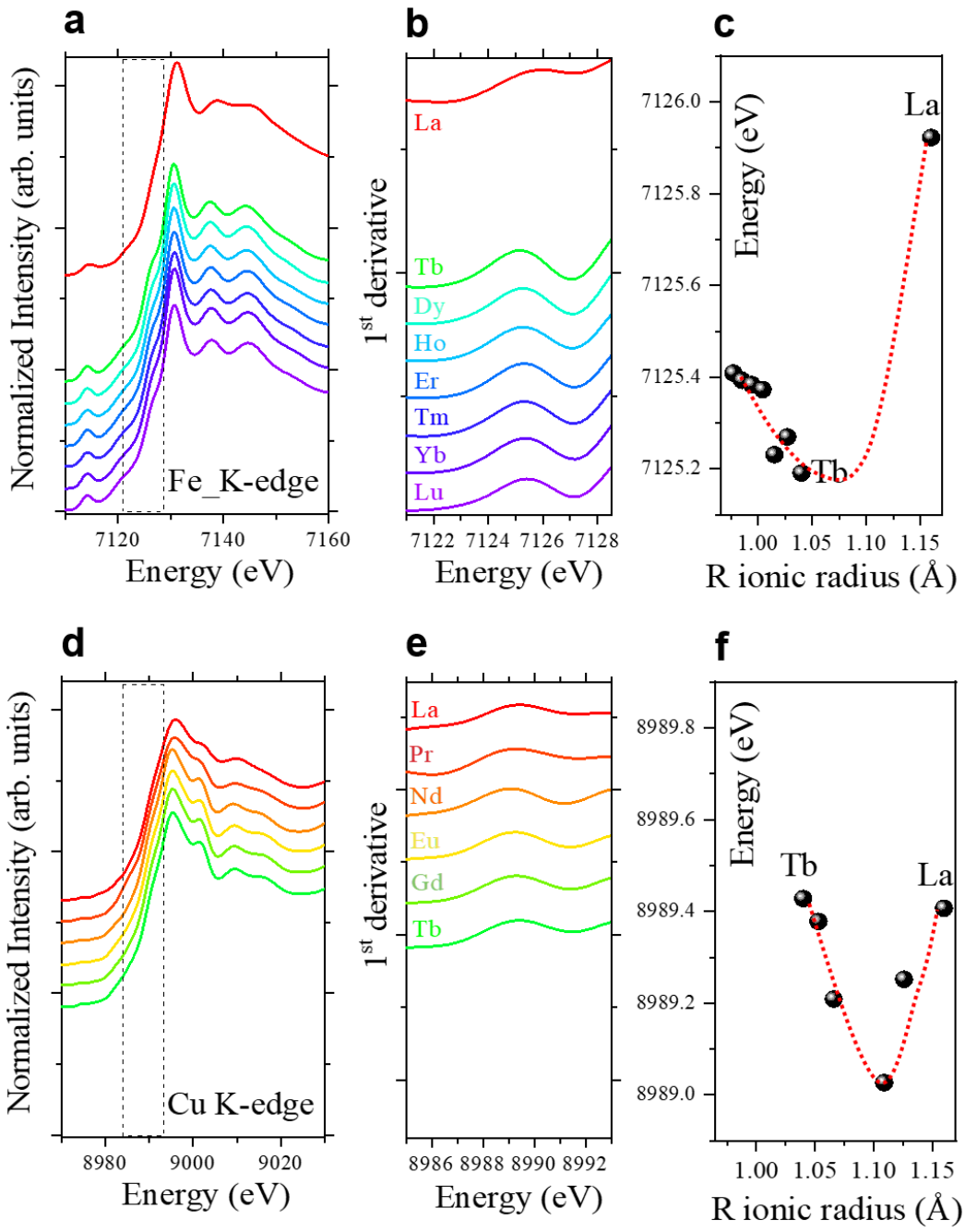

Fig. S8. **Fe and Cu *K*-edges of *R*BaCuFeO$_{5+\delta}$ layered perovskites.** (a) Accessible Fe *K*-edges. (b) Fe *K*-edges 1st derivative. (c) Evolution of the Fe *K*-edge 1st derivative maximum with the *R* ionic radius. (d) Accessible Cu *K*-edges. (e) Cu *K*-edges 1st derivative. (f) Evolution of the Cu *K*-edge 1st derivative maximum with the *R* ionic radius. All spectra were measured at the SuperXAS beamline[10] (SLS, PSI) using the Total Fluorescence Yield mode (TFY). The red dotted lines are guides for the eye.

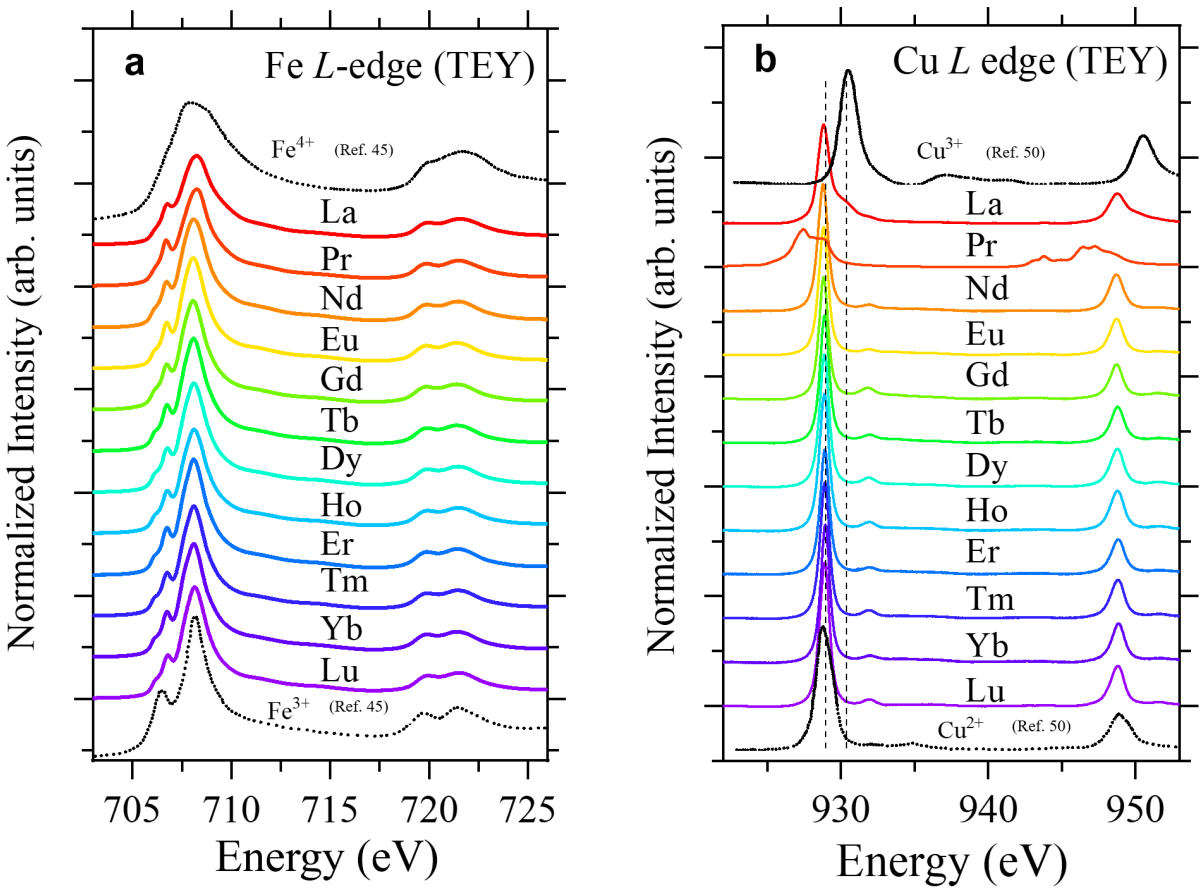

Fig. S9. **Fe and Cu *L*-edges of *R*BaCuFeO$_{5+\delta}$ layered perovskites.** (a) Fe *L*-edges. (b) Cu *L*-edges. The figure illustrates the evolution of the L_3 and L_2 intensities along the series. The black curves are reference Fe^{3+}, Fe^{4+}, Cu^{2+} and Cu^{3+} spectra from refs. 45 and 50 (main text). All *R*BaCuFeO$_{5+\delta}$ spectra were measured at the Xtreme beamline[11] (SLS, PSI) using the Total Electron Yield mode (TEY).

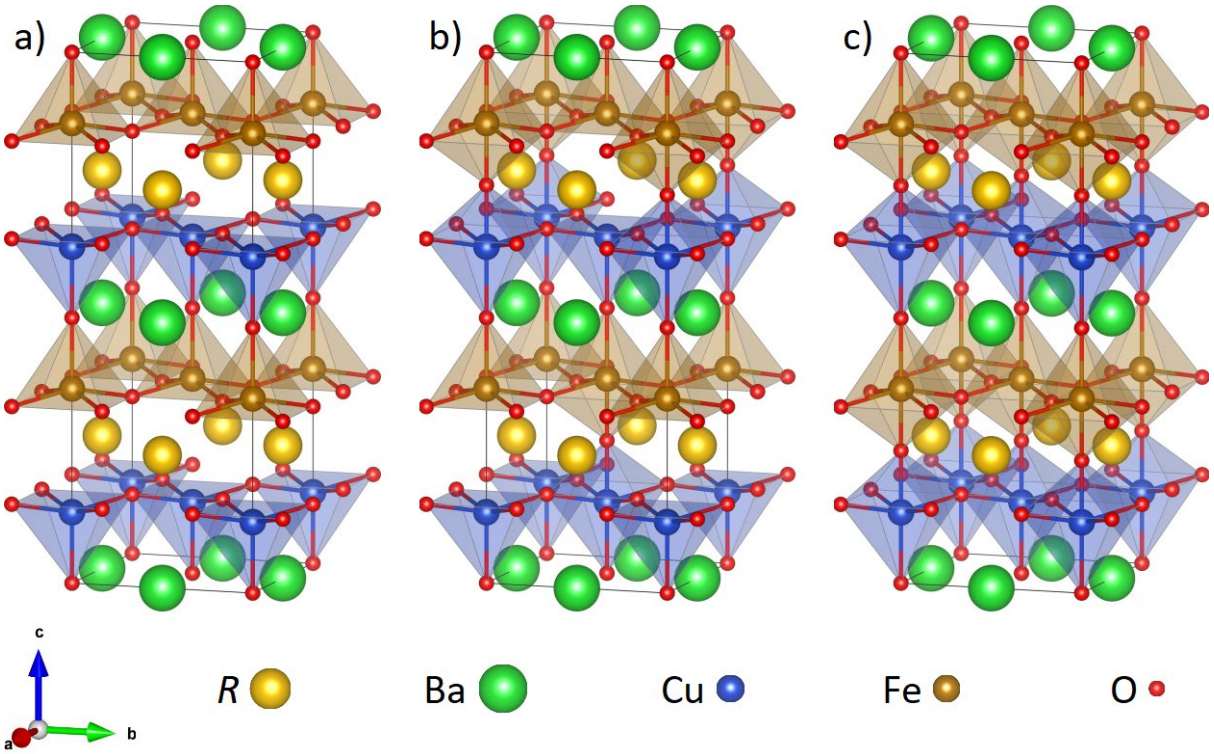

Fig. S10. **Model structures employed in the DFT calculations.** a) *R*BaCuFeO$_5$, b) *R*BaCuFeO$_{5.5}$, and c) *R*BaCuFeO$_6$. The cell volume is $\sqrt{2}\boldsymbol{a} \cdot \sqrt{2}\boldsymbol{a} \cdot 2\boldsymbol{c}$.

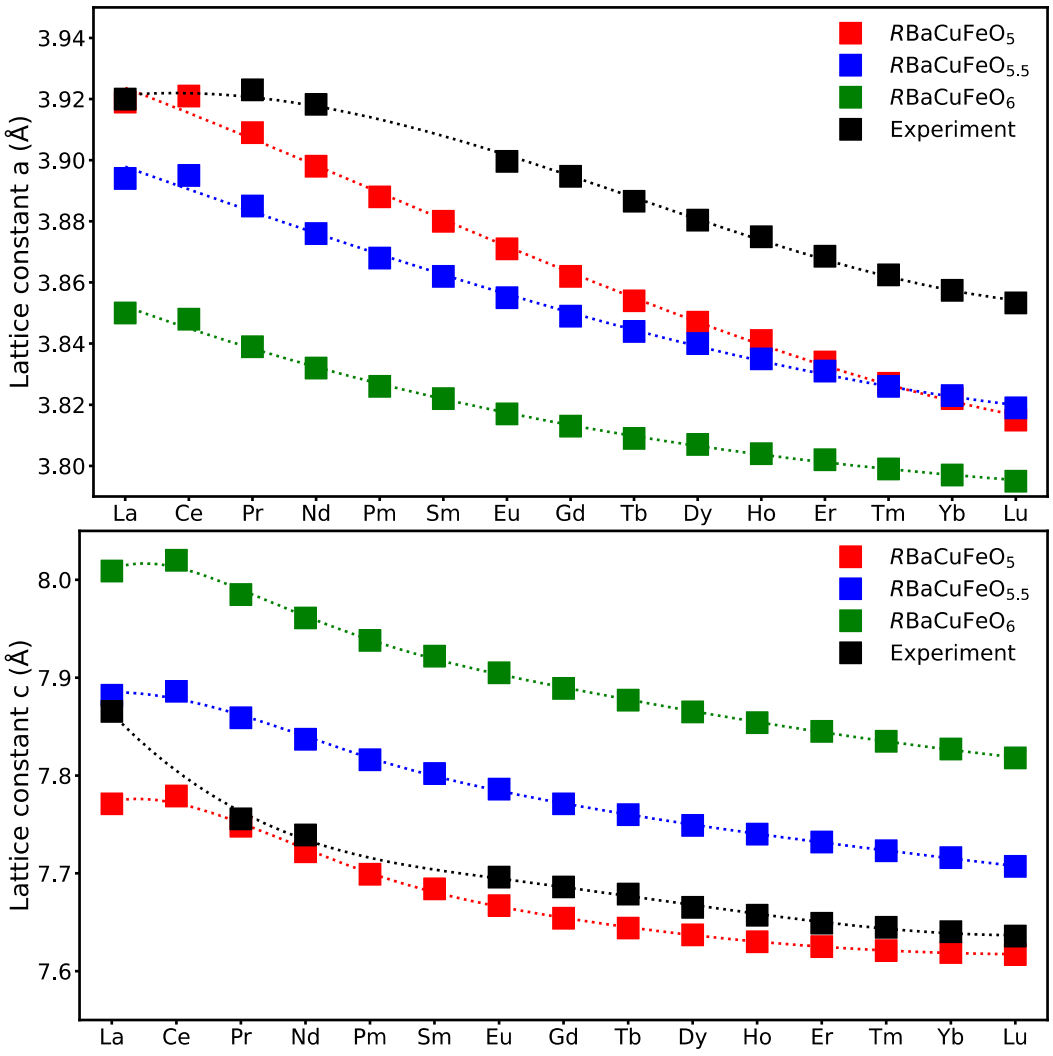

Fig. S11. **Measured versus calculated lattice parameters.** Comparison of the experimental lattice parameters with those calculated for the *R*BaCuFeO$_x$ model systems with x = 0, 0.5 and 1 shown in Fig. S10.

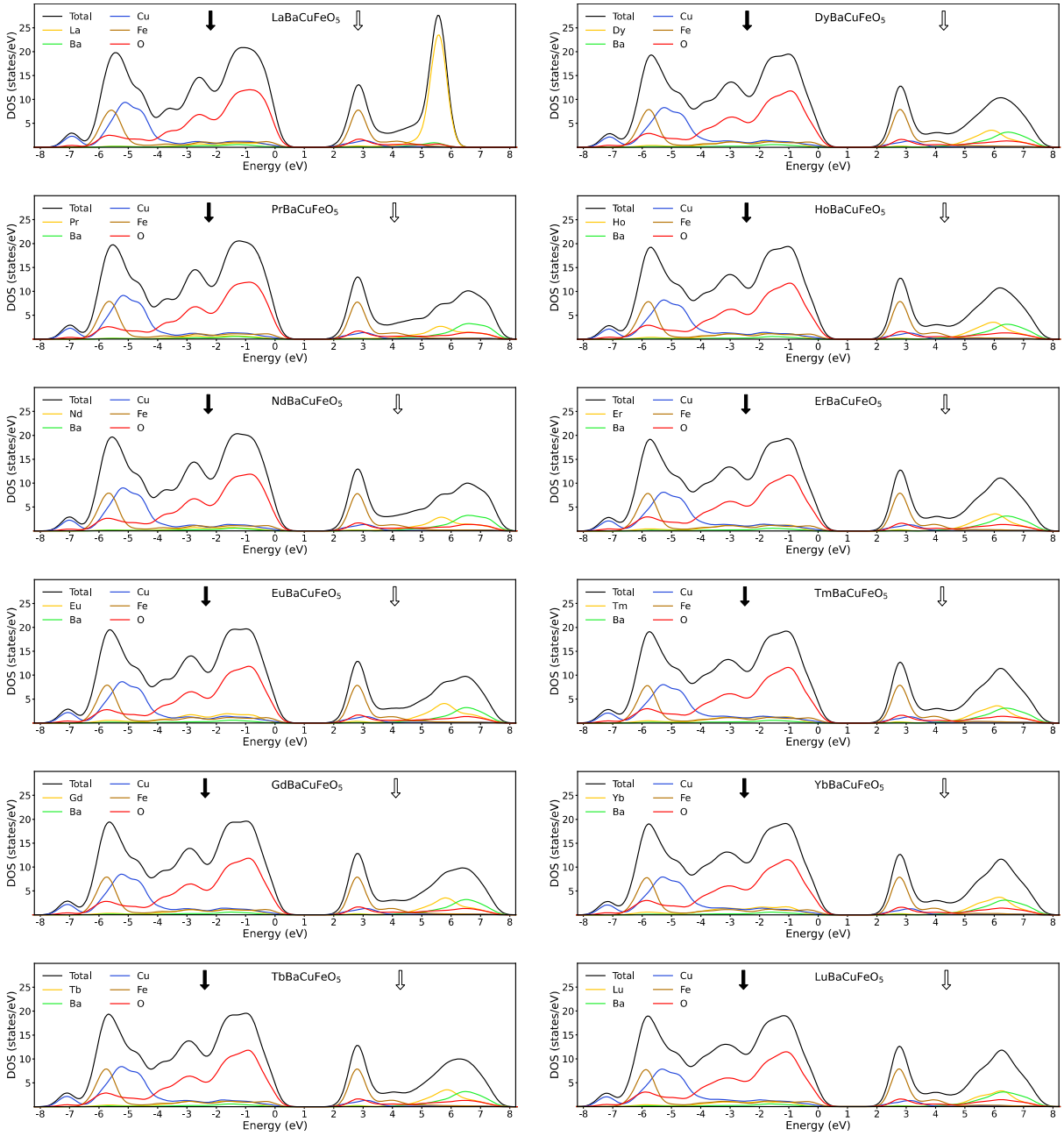

Fig. S12. **Calculated DOS for the *R*BaCuFeO$_5$ samples.** The partial DOS for each cation/anion is displayed using the same color code as in Fig. 1a. For all materials (including *R* = La), the calculations have been conducted assuming perfect *R*/Ba order along the **c** axis using the supercell shown in Fig. S10. The arrows indicate the centroids of the occupied (black) and the unoccupied (white) O(2*p*) orbitals.

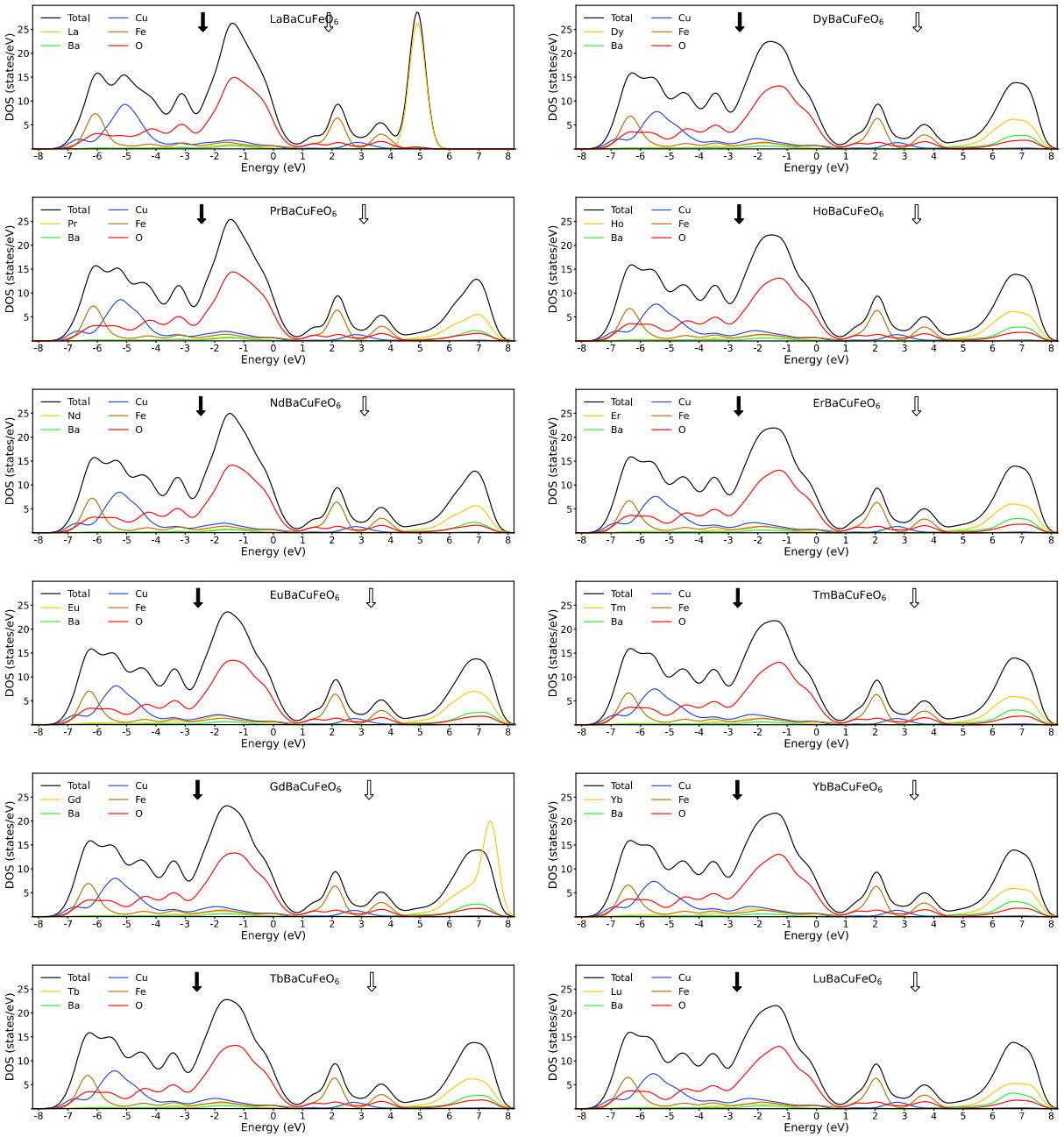

Fig. S13. **Calculated DOS for the *R*BaCuFeO$_6$ samples.** The partial DOS for each cation/anion is displayed using the same color code as in Fig. 1a. For all materials (including *R* = La), the calculations have been conducted assuming perfect *R*/Ba order along the **c** axis using the supercell shown in Fig. S10. The arrows indicate the centroids of the occupied (black) and the unoccupied (white) O(2*p*) orbitals.

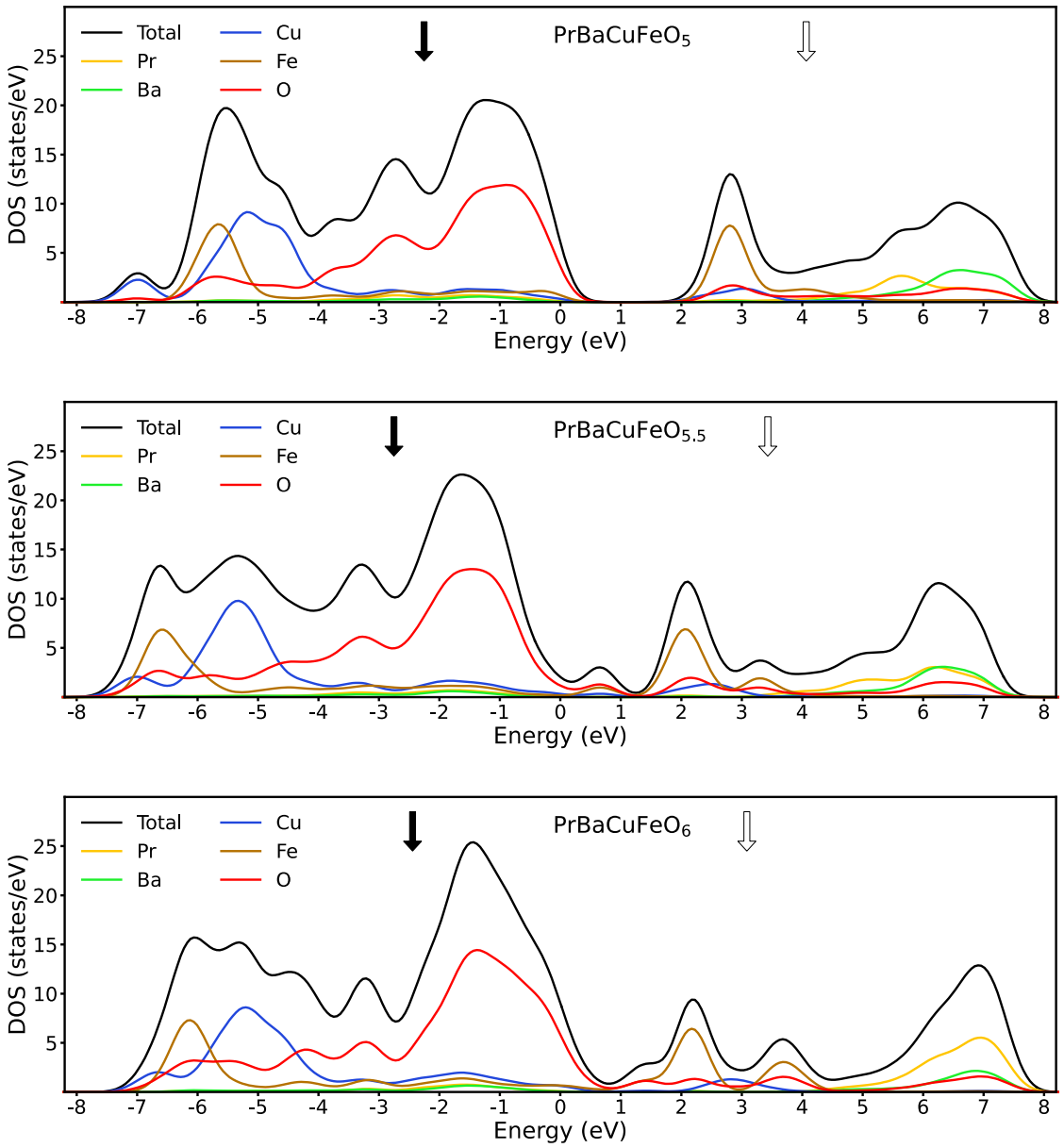

Fig. S14. **Calculated DOS for the $PrBaCuFeO_5$, $PrBaCuFeO_{5.5}$ and $PrBaCuFeO_6$.** The partial DOS for each cation/anion is displayed using the same color code as in Fig. 1a. The figure illustrates the progressive closing of the gap upon incorporation of oxygen in the structure. The arrows indicate the centroids of the occupied (black) and the unoccupied (white) O(2*p*) orbitals. The calculations have been conducted assuming perfect *R*/Ba order along the **c** axis using the supercells shown in Fig. S10.

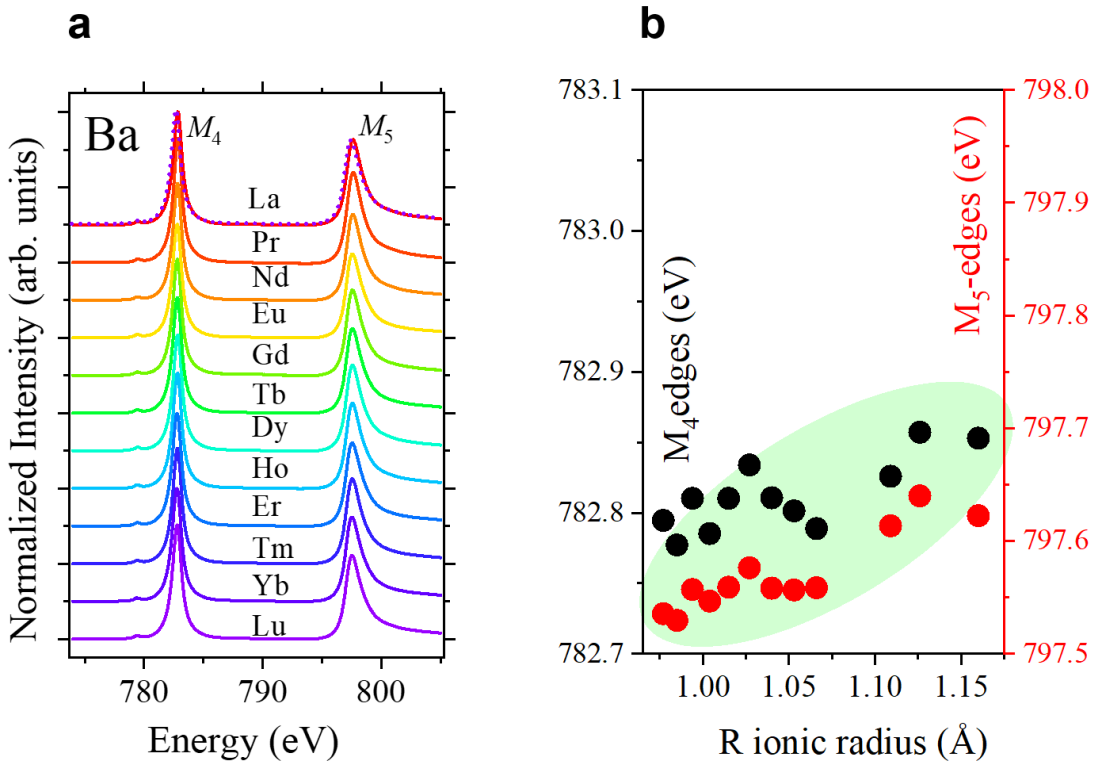

Fig. S15. **Ba *M*-edges of *R*BaCuFeO$_{5+\delta}$ layered perovskites.** (a) Ba *M*-edges measured at the Xtreme beamline[11] (SLS, PSI) using the Total Electron Yield mode (TEY). The dashed line is the spectrum of the sample with *R* = Lu. It was superimposed to that with *R* = La to illustrate the practical invariance of the Ba *M*-edges along the series. After background subtraction, all spectra were area-normalized as described in the Materials and Methods section (b) Energy at the maximum of the M_5 (left) and M_4 (right) lines.

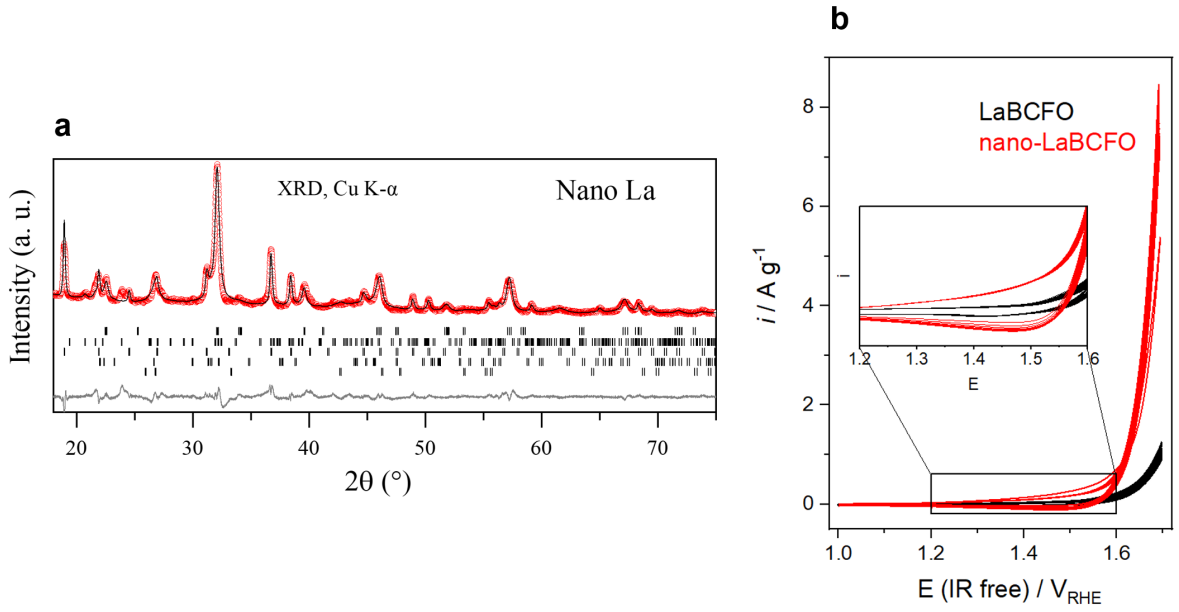

Fig. S16. Characterization of the LaBaCuFeO$_{5+\delta}$ nanoparticles. **(a)** Laboratory powder X-ray diffraction patterns (Cu *K*α) of the nano-LaBaCuFeO$_{5+\delta}$ sample. Red crosses: experimental data. Black lines: refined profile. Grey line: difference between the observed and calculated patters. The ticks indicate the positions of the Bragg reflections associated to the different phases present in the sample. Majoritary phase: LaBaCuFeO$_{5+\delta}$ (1st row, Table S3, ~58% in weight). Impurity phases: Cu(NO$_3$)$_2$, (2nd row, ICSD: 28477, ~11% in weight); Ba(NO$_3$)$_2$ (3rd row, ICSD: 95594, ~21% in weight). Traces (Lebail-fitted): LaBa$_2$Cu$_3$O$_{6+\delta}$ (4st row, ICSD:64632); BaO$_2$ (5th row, ICSD:80750). The weight fractions are those provided by the FullProf Suite Rietveld software. However, they should be considered with caution due to the difficulties for refining the powder diffraction data, which are affected by a strong broadening of the Bragg reflections and by the presence of preferred orientations. **(b)** Comparison between the cyclic voltammogram of the bulk (black) and nano (red) LaBCFO samples.

Tables S1 to S3

Table S1. Physical and electrochemical properties of *R*BaCuFeO$_{5+\delta}$ layered perovskites: R^{3+} electronic configuration, electric conductivity σ, Tafel slopes, OER gravimetric activity at 1.65 V_{RHE}, and overpotentials (η) at 10 mAg^{-1}.

R	R^{3+} electr. config.	σ / S cm^{-1}	*Slope / V dec^{-1}*	*i* @ 1.65 V_{RHE} / mA g^{-1}	η@ 10 mA g^{-1} / V_{RHE}
Lu	[Xe]4f^{14}	$3\cdot10^{-10}$	0.084(1)	82(4)	0.639(2)
Yb	[Xe]4f^{13}	$3\cdot10^{-9}$	0.174(6)	24(4)	0.65(2)
Tm	[Xe]4f^{12}	$8\cdot10^{-11}$	0.080(2)	91(8)	0.639(4)
Er	[Xe]4f^{11}	$2\cdot10^{-10}$	0.104(3)	50(6)	0.643(8)
Ho	[Xe]4f^{10}	$4\cdot10^{-10}$	0.085(2)	97(7)	0.632(4)
Dy	[Xe]4f^{9}	$5\cdot10^{-10}$	0.094(2)	68(5)	0.637(4)
Tb	[Xe]4f^{8}	$2\cdot10^{-10}$	0.081(1)	111(4)	0.631(2)
Gd	[Xe]4f^{7}	$4\cdot10^{-10}$	0.074(2)	186(12)	0.622(4)
Eu	[Xe]4f^{6}	$7\cdot10^{-10}$	0.080(3)	148(15)	0.622(6)
Nd	[Xe]4f^{3}	$1\cdot10^{-6}$	0.089(2)	181(10)	0.605(4)
Pr	[Xe]4f^{2}	$2\cdot10^{-6}$	0.083(3)	166(15)	0.614(5)
La	[Xe]4f^{0}	$7\cdot10^{-4}$	0.096(2)	255(11)	0.582(3)
Nano-La	[Xe]4f^{0}	$1\cdot10^{-12}$	0.071(2)	1281(33)	0.565(2)

Table S2. RT lattice parameters of *R*BaCuFeO$_{5+\delta}$ layered perovskites. *R* ionic radii (in 8-fold coordination), refined lattice parameters, *c*/2*a* ratios and diffraction domain average sizes *D* (Scherrer formula) obtained from the Rietveld fits of laboratory X-ray diffraction data (Cu K_α) for the *R*BaCuFeO$_{5+\delta}$ ceramic samples and the LaBaCuFeO$_{5+\delta}$ nanopowder.

***R* cation**	***R*$_{ionic}$ (Å)[17]**	***a* (Å)**	***c* (Å)**	***c* / *2a***	***D (nm)***
Lu	0.977	3.85332(1)	7.63580(2)	0.99081(1)	610.9(7)
Yb	0.985	3.85743(1)	7.64030(1)	0.99034(1)	395.2(4)
Tm	0.994	3.86248(1)	7.64477(1)	0.98962(1)	415.0(6)
Er	1.004	3.86856(1)	7.64897(2)	0.98861(1)	179.8(2)
Ho	1.015	3.87494(1)	7.65717(1)	0.98804(1)	226.6(2)
Dy	1.027	3.88041(1)	7.66522(2)	0.98768(1)	343.6(5)
Tb	1.04	3.88657(1)	7.67876(1)	0.98786(1)	295.3(4)
Gd	1.053	3.89475(1)	7.68605(1)	0.98672(1)	552.0(6)
Eu	1.066	3.89960(1)	7.69604(2)	0.98677(1)	200.3(3)
Nd	1.109	3.91826(1)	7.73922(1)	0.98758(1)	507.3(6)
Pr	1.126	3.92300(1)	7.75569(4)	0.98849(1)	273.0(2)
La	1.16	3.91998(3)	7.86539(7)	1.00324(1)	502.9(6)
La-nano	1.16	3.9362(2)	7.9174(7)	1.0057(1)	15.77(3)

Table S3 (next page). Structural data of *R*BaCuFeO$_{5+\delta}$ layered perovskites. The lattice parameters, atomic coordinates, fractional oxygen site occupations and anisotropic mean-square displacements were obtained from the Rietveld fits of high-resolution PND data (HRPT, λ = 1.15 Å).

R* cation / *Space group	**Tb / *P4mm***	**Nd / *P4/mmm***	**Pr / *P4/mmm***	**La / *P4/mmm***
a (Å)	3.88496(4)	3.91582(7)	3.92154(7)	3.91371(15)
c (Å)	7.67540(11)	7.73693(16)	7.75351(17)	7.8590(3)
Ba1	**1a (0 0 *z*)**	**1a (0 0 0)**	**1a (0 0 0)**	**1a (0 0 0)**
Occ. (fractional)	1	1	1	0.55(7)
z	-0.005(9)	-	-	-
U_{11} (Å^2)	0.0073(4)	0.0072(5)	0.0077(6)	0.0175(5)
U_{33} (Å^2)	0.021(6)	0.0175(14)	0.0194(13)	0.0051(6)
R1				**1a (0 0 0)**
Occ. (fractional)				0.45(7)
z				-
U_{11} (Å^2)				0.0175(5)
U_{33} (Å^2)				0.0051(6)
Ba2				**1b (0 0 ½)**
Occ. (fractional)				0.45(7)
z				-
U_{11} (Å^2)				0.0175(5)
U_{33} (Å^2)				0.0051(6)
R2	**1a (0 0 *z*)**	**1b (0 0 ½)**	**1b (0 0 ½)**	**1b (0 0 ½)**
Occ. (fractional)	1	1	1	0.55(7)
z	0.501(5)	-	-	-
U_{11} (Å^2) / U_{iso} (Å^2)	0.00419(16)	0.0053(4)	0.0083(8)	0.0175(5)
U_{33} (Å^2)	-	-	-	0.0051(6)
Cu1	**1b (½ ½ *z*)**	**2h (½ ½ *z*)**	**2h (½ ½ *z*)**	**2h (½ ½ *z*)**
Occ. (fractional)	0.491(13)	0.5	0.5	0.5
z	0.2810(4)	0.2743(4)	0.2719(3)	0.25
U_{11} (Å^2) / U_{iso} (Å^2)	0.00421(13)	0.00503(16)	0.00511(13)	0.0158(4)
U_{33} (Å^2)	-	-	-	0.0014(2)
Fe1	**1b (½ ½ *z*)**	**2h (½ ½ *z*)**	**2h (½ ½ *z*)**	**2h (½ ½ *z*)**
Occ. (fractional)	0.509(13)	0.5	0.5	0.5
z	0.2530(4)	0.2490(4)	0.2485(3)	0.25
U_{11} (Å^2) / U_{iso} (Å^2)	0.00421(13))	0.00503(16)	0.00511(13)	0.0158(4)
U_{33} (Å^2)	-	-	-	0.0014(2)
Cu2	**1b (½ ½ *z*)**			
Occ. (fractional)	0.509(13)			
z	0.7187(4)			
U_{iso} (Å^2)	0.00421(13)			
Fe2	**1b (½ ½ *z*)**			
Occ. (fractional)	0.491(13)			
z	0.7470(4)			
U_{iso} (Å^2)	0.00421(13)			
***O1*$_{apical}$**	**1b (½ ½ *z*)**	**1c (½ ½ 0)**	**1c (½ ½ 0)**	**1c (½ ½ 0)**
Occ. (fractional)	1	1	1	0.750(12)
z	0	-	-	
U_{11} (Å^2)	0.0088(4)	0.0108(5)	0.0161(7)	0.047(3)
U_{33} (Å^2)	0.0195(12)	0.0163(11)	0.0152(10)	0.0070(12)
***O2*$_{basal}$**	**2c (½ 0 *z*)**	**4i (0 ½ *z*)**	**4i (0 ½ *z*)**	**4i (0 ½ *z*)**
z	0.315(3)	0.30484(13)	0.30190(12)	0.2558(9)
U_{11} (Å^2)	0.0077(3)	0.0068(4)	0.0073(4)	0.069(3)
U_{22} (Å^2)	0.0052(3)	0.0075(4)	0.0080(4)	0.0239(10)
U_{33} (Å^2)	0.0119(5)	0.0155(4)	0.0190(4)	0.0189(11)
***O2'*$_{basal}$**	**2c (½ 0 *z*)**			
z	0.690(3)			
U_{11} (Å^2)	0.0077(3)			
U_{22} (Å^2)	0.0052(3)			
U_{33} (Å^2)	0.0119(5)			
***O3*$_{apical}$**		**1d (½ ½ ½)**	**1d (½ ½ ½)**	**1d (½ ½ ½)**
Occ. (fractional)		0.08100(8)	0.150(5)	0.7386(11)
U_{11} (Å^2) / U_{iso} (Å^2)		0.01205(6)	0.020(2)	0.047(3)
U_{33} (Å^2)		-	-	0.0070(12)
***Chi*^{2}**	3.01	1.46	1.87	2.40
***R*$_p$**	2.44	3.45	3.24	4.56
***R*$_{wp}$**	3.13	4.35	4.15	5.97
***R*$_{Bragg}$**	3.82	2.71	2.88	6.62

Supplementary References

1. E. Fabbri, M. Nachtegaal, T. Binninger, X. Cheng, B.-J. Kim, J. Durst, F. Bozza, T. Graule, R. Schäublin, L. Wiles, M. Pertoso, N. Danilovic, K. E. Ayers and T. J. Schmidt, *Nature Materials*, 2017, **16**, 925-931.
2. D. Aegerter, M. Borlaf, E. Fabbri, A. H. Clark, M. Nachtegaal, T. Graule and T. J. Schmidt, *Catalysts*, 2020, **10**, 984.
3. J. Rodríguez-Carvajal, *Physica B: Condensed Matter*, 1993, **192**, 55-69.
4. P. Fischer, G. Frey, M. Koch, M. Könnecke, V. Pomjakushin, J. Schefer, R. Thut, N. Schlumpf, R. Bürge, U. Greuter, S. Bondt and E. Berruyer, *Physica B: Condensed Matter*, 2000, **276-278**, 146-147.
5. M. Morin, A. Scaramucci, M. Bartkowiak, E. Pomjakushina, G. Deng, D. Sheptyakov, L. Keller, J. Rodriguez-Carvajal, N. A. Spaldin, M. Kenzelmann, K. Conder and M. Medarde, *Phys Rev B*, 2015, **91**, 064408.
6. M. Morin, E. Canevet, A. Raynaud, M. Bartkowiak, D. Sheptyakov, V. Ban, M. Kenzelmann, E. Pomjakushina, K. Conder and M. Medarde, *Nat Commun*, 2016, **7**, 13758.
7. T. Shang, E. Canévet, M. Morin, D. Sheptyakov, M. T. Fernández-Díaz, E. Pomjakushina and M. Medarde, *Science Advances*, 2018, **4**, eaau6386.
8. X. D. Zhang, A. Romaguera, O. Fabelo, F. Fauth, J. Herrero-Martin and J. L. Garcia-Munoz, *Acta Mater*, 2021, **206**.
9. A. Romaguera, X. D. Zhang, O. Fabelo, F. Fauth, J. Blasco and J. L. Garcia-Munoz, *Phys Rev Res*, 2022, **4**, 043188.
10. O. Muller, M. Nachtegaal, J. Just, D. Lutzenkirchen-Hecht and R. Frahm, *J Synchrotron Radiat*, 2016, **23**, 260-266.
11. C. Piamonteze, U. Flechsig, S. Rusponi, J. Dreiser, J. Heidler, M. Schmidt, R. Wetter, M. Calvi, T. Schmidt, H. Pruchova, J. Krempasky, C. Quitmann, H. Brune and F. Nolting, *J Synchrotron Radiat*, 2012, **19**, 661-674.
12. G. Kresse and J. Furthmuller, *Phys Rev B*, 1996, **54**, 11169-11186.
13. G. Kresse and D. Joubert, *Phys Rev B*, 1999, **59**, 1758-1775.
14. J. P. Perdew, A. Ruzsinszky, G. I. Csonka, O. A. Vydrov, G. E. Scuseria, L. A. Constantin, X. L. Zhou and K. Burke, *Phys Rev Lett*, 2008, **100**.
15. S. L. Dudarev, G. A. Botton, S. Y. Savrasov, C. J. Humphreys and A. P. Sutton, *Phys Rev B*, 1998, **57**, 1505-1509.
16. A. M. Ganose, Jackson, A.J., Scanlon, D.O., *JOSS*, 2018, **3**, 717.
17. R. Shannon, *Acta Crystallographica Section A*, 1976, **32**, 751-767.